

Two Bipolar Outflows and Magnetic Fields in a Multiple Protostar System, L1448 IRS 3

Woojin Kwon, Leslie W. Looney, Richard M. Crutcher¹, and Jason M. Kirk²

Department of Astronomy, University of Illinois at Urbana-Champaign, 1002 W. Green St., Urbana, IL 61801

wkwon@astro.uiuc.edu

ABSTRACT

We performed spectral line observations of CO $J = 2 \rightarrow 1$, $^{13}\text{CO } J = 1 \rightarrow 0$, and $\text{C}^{18}\text{O } J = 1 \rightarrow 0$ and polarimetric observations in the $\lambda = 1.3$ mm continuum and CO $J = 2 \rightarrow 1$ toward a multiple protostar system, L1448 IRS 3, in the Perseus molecular complex at a distance of ~ 250 pc, using the BIMA array. In the $\lambda = 1.3$ mm continuum, two sources (IRS 3A and 3B) were clearly detected with estimated envelope masses of 0.21 and $1.15 M_{\odot}$, and one source (IRS 3C) was marginally detected with an upper mass limit of $0.03 M_{\odot}$. In CO $J = 2 \rightarrow 1$, we revealed two outflows originating from IRS 3A and 3B. The masses, mean number densities, momentums, and kinetic energies of outflow lobes were estimated. Based on those estimates and outflow features, we concluded that the two outflows are interacting and that the IRS 3A outflow is nearly perpendicular to the line of sight. In addition, we estimated the velocity, inclination, and opening of the IRS 3B outflow using Bayesian statistics. When the opening angle is $\sim 20^\circ$, we constrain the velocity to $\sim 45 \text{ km s}^{-1}$ and the inclination angle to $\sim 57^\circ$. Linear polarization was detected in both the $\lambda = 1.3$ mm continuum and CO $J = 2 \rightarrow 1$. The linear polarization in the continuum shows a magnetic field at the central source (IRS 3B) perpendicular to the outflow direction, and the linear polarization in the CO $J = 2 \rightarrow 1$ was detected in the outflow regions, parallel or perpendicular to the outflow direction. Moreover, we comprehensively discuss whether the binary system of IRS 3A and 3B is gravitationally bound, based on the velocity differences detected in $^{13}\text{CO } J = 1 \rightarrow 0$ and $\text{C}^{18}\text{O } J = 1 \rightarrow 0$ observations and on the outflow features. The specific angular momentum of the system was estimated as $\sim 3 \times 10^{20} \text{ cm}^2 \text{ s}^{-1}$, comparable to the values obtained from previous studies on binaries and molecular clouds in Taurus.

¹ Additionally at National Center for Supercomputing Applications

² Currently at Department of Physics and Astronomy, Cardiff University

Subject headings: ISM: individual (L1448 IRS 3) — magnetic fields — polarization — stars: outflows

1. Introduction

L1448 is a dark cloud located approximately one degree southwest from NGC 1333 in the Perseus cloud complex at a distance of ~ 250 pc (e.g. Enoch et al. 2006). Three infrared sources were observed by the Infrared Astronomical Satellite (IRAS) and denoted as IRS 1, IRS 2, and IRS 3 by Bachiller & Cernicharo (1986). Due to its brightness in the IRAS bands, IRS 3 has been focused on more than the others. Meanwhile, Bachiller et al. (1990, 1995) revealed a well-collimated, large outflow originating from L1448-mm, located $70''$ southeast of L1448 IRS 3. In fact, IRS 3 is overlapped with the blueshifted lobe of the outflow. Curiel et al. (1990) detected the L1448-mm continuum source and two sources separated by $7''$ in the L1448 IRS 3 region, using the Very Large Array (VLA) at $\lambda = 6$ and 2 cm wavelengths. They named the sources L1448 C (for Center) and L1448 N(A) and N(B) (for North) for L1448-mm and the two sources in IRS 3, respectively. Terebey & Padgett (1997) detected another source $20''$ northwest of the two IRS 3 sources at $\lambda = 2.7$ mm continuum, using the Owens Valley Radio Observatory (OVRO) millimeter interferometer. Looney et al. (2000) resolved all three sources in IRS 3 with high resolution Berkeley Illinois Maryland Association (BIMA) observations at $\lambda = 2.7$ mm continuum. In this paper, we call these sources L1448-mm and L1448 IRS 3A, 3B, and 3C, using IAU nomenclature.

In addition to the multiplicity of young sources in L1448 IRS 3, multiple outflows in the region have been suggested in previous studies. Bachiller et al. (1990, 1995) suggested an outflow originating from IRS 3B, since they detected a redshifted component in the blueshifted lobe of the mm-source outflow and since IRS 3B is the brightest source at mm wavelengths. In contrast, Curiel et al. (1990) suggested that the outflow was driven by IRS 3A, based on a spectral index of 0.2, similar to thermal jet models (e.g. Reynolds 1986), and coincident H₂O maser observations. Davis & Smith (1995) and Eislöffel (2000) presented H₂ emission images showing shocked regions. They suggested up to three outflows in the IRS 3 region from collimated features in the images. Several Herbig-Haro objects were also detected and explained as outflows driven by the three IRS 3 sources (Bally et al. 1997). Wolf-Chase et al. (2000) suggested two outflows from IRS 3A and 3B, based on previous studies and their large-scale maps of CO $J = 1 \rightarrow 0$ emission. Moreover, Girart & Acord (2001) reported a well collimated redshifted component detected along a line of position angle 110° from IRS 3B in SiO $J = 2 \rightarrow 1$ emission. These previous studies, however, could not clearly show the outflow features relative to the sources due to a lack of angular

resolution and the inherent complexity of the region.

Theoretical studies have suggested that magnetic fields play key roles in the outflows of protostars as well as star formation itself. Observations of magnetic morphology and strength are possible using the Zeeman effect (e.g. Crutcher 1999) and linear polarization of dust emission and spectral lines (e.g. Girart et al. 1999). Crutcher et al. (2004) recently estimated the magnetic strength as well as morphology, from linear polarization of dust emission in three prestellar cores (starless cores) using the Chandrasekhar-Fermi method (Chandrasekhar & Fermi 1953). In the case of magnetic fields related to protostars (Class 0 sources) with outflows, Girart et al. (1999) detected linear polarization in the $\lambda = 1.3$ mm dust emission and CO $J = 2 \rightarrow 1$ spectral line. Their study was unique for low mass protostars with outflows.

In this paper, we present polarimetric observations in the $\lambda = 1.3$ mm continuum and CO $J = 2 \rightarrow 1$ showing two outflows and magnetic fields in the L1448 IRS 3 region, using the BIMA array. Moreover, ^{13}CO $J = 1 \rightarrow 0$ and C^{18}O $J = 1 \rightarrow 0$ observation results are presented. We argue that the binary system of L1448 IRS 3A and 3B is gravitationally bound, using these ^{13}CO and C^{18}O observations.

2. Observation and data reduction

We performed $\lambda = 1.3$ mm continuum and CO $J = 2 \rightarrow 1$ polarimetric observations toward L1448 IRS 3, using nine of the 10 antennas in the BIMA array¹ (Welch et al. 1996). The data were obtained on 2003 October 17, 25, 26, and November 13 in C configuration and integrated for 9 hours except October 17, which was 3 hours due to weather. To get $\lambda = 1.3$ mm continuum data as well as CO $J = 2 \rightarrow 1$ spectral line, a correlator mode with 4 windows of 100 MHz bandwidth each in both sidebands was used. This mode gives $\sim 4 \text{ km s}^{-1}$ channel width for the CO $J = 2 \rightarrow 1$ spectral line. The first window of the upper side band was centered at the rest frequency of CO $J = 2 \rightarrow 1$, 230.538 GHz. The synthesized beam, obtained through natural weighting, is around $2''.5 \times 4''.5$.

0237+288 was used as a secondary flux calibrator as well as a phase calibrator; Uranus was the primary flux calibrator. We set the flux of 0237+288 of all data on the value determined from Uranus observed October 25, the best data set. As the 0237+288 flux is

¹The BIMA Array was operated by the Berkeley Illinois Maryland Association under funding from the National Science Foundation. BIMA has since combined with the Owens Valley Radio Observatory millimeter interferometer, moved to a new higher site, and was recommissioned as the Combined Array for Research in Millimeter-wave Astronomy (CARMA) in 2006.

not variable in such a short period (40 days), it is arguably the most consistent combination of the data. The flux of 0237+288 estimated by the primary flux calibrator is 1.33 Jy; our flux calibration is estimated at a 20% absolute uncertainty.

Each antenna of the BIMA array has a quarter-wave plate in the front of the linearly polarized feed for polarimetric observations. The quarter-wave plate gives left (L) or right (R) circular polarizations and the cross correlations (LL, RR, LR, RL) enable the calculation of the Stokes parameters. To obtain quasi-simultaneous measurements of dual polarizations, antennas switch to measure L or R circular polarization following a fast Walsh function. The data are averaged over the Walsh cycle. The details on the BIMA polarimetric instrument can be found in Rao (1999). In the polarimetry observations, instrumental leakage must be compensated. The leakage terms are $\sim 5\%$ at $\lambda \sim 1$ mm and constant until quarter-wave plates are reinstalled (Rao 1999; Rao et al. 1998). In addition, they are strongly dependent on frequency. We used 3C279 data observed on 2003 March 4 at the same frequency (230.538 GHz) to get the leakage terms.

MIRIAD (Sault et al. 1995) was used to reduce our data. First, we applied gains obtained from calibrators and constructed models for each observation date. Data of each observation date were self-calibrated with the model constructed from their own data. After combining the individually self-calibrated data, we constructed a combined model. Finally, all data were individually self-calibrated again with this model and combined to the final result.

^{13}CO $J = 1 \rightarrow 0$ ($\nu_{rest} = 110.201$ GHz) and C^{18}O $J = 1 \rightarrow 0$ ($\nu_{rest} = 109.782$ GHz) data were obtained on 2004 April in C configuration of the BIMA array. These two spectral lines were observed simultaneously with a channel width of $\sim 1 \text{ km s}^{-1}$ and synthesized beam size of $\sim 8'' \times 7''$. Uranus was used as a primary flux calibrator and 0336+323 as a phase calibrator and a secondary flux calibrator. The estimated 0336+323 flux was 1.65 Jy. Again, this flux calibration is estimated at a 20% absolute uncertainty.

Submillimeter continuum observations of L1448 IRS 3 at 850 μm were accessed from the JCMT data archive. They had originally been observed with SCUBA (Holland et al. 1999) on the JCMT on Mauna Kea, during the evenings of 1999 August 28 (6 pointings), 2000 January 3 (7 pointings), and 2000 February 24 (2 pointings). SCUBA was used with the SCUBAPOL (Greaves et al. 2003) polarimeter, which uses a rotating half-wave plate and fixed analyzer. The wave plate is stepped through sixteen positions (each offset from the last by 22.5°) and a Nyquist-sampled image (using a 16-point jiggle pattern) is taken at each wave plate position (Greaves et al. 2003). The observations were carried out while chopping the secondary mirror 120 arcsec in azimuth at 7 Hz and synchronously detecting the signal, thus rejecting sky emission. The integration time per point in the jiggle cycle was

1 second, in each of the left and right telescope beams of the dual-beam chop. The total on-source integration time per complete cycle was 512 seconds. The instrumental polarization (IP) of each bolometer was measured on the planets Mars and Uranus. This was subtracted from the data before calculating the true source polarization. The mean IP was found to be $0.93 \pm 0.27\%$. The submillimeter zenith opacity for atmospheric extinction removal was determined by comparison with the 1.3-mm sky opacity (Archibald et al. 2002).

3. Dust continuum emission

Looney et al. (2000) revealed three Class 0 sources in this region in the $\lambda = 2.7$ mm continuum with high resolution BIMA observation and denominated as L1448 IRS 3A, 3B, and 3C (hereafter IRS 3A, 3B, and 3C). Note that some authors used L1448 N(A), N(B), and NW, respectively (Terebey & Padgett 1997; Barsony et al. 1998). Ciardi et al. (2003) reported a mid-infrared ($10 \sim 25 \mu\text{m}$) observation of IRS 3A and 3B. They suggested that IRS 3A and 3B are Class I and Class 0 sources respectively, based on a comparison of the envelope and central source masses. On one hand, IRS 3A and 3B could be a “coeval” binary system with different central masses and so be evolving at different rates. On the other, they may be evolving at a same rate under different environments due to interaction, a mass flow from one to the other. Although we do not focus on distinguishing the two cases, we discuss the binarity (i.e. if the two sources are gravitationally bound) later, which is a basis for the two ideas.

Figure 1 shows the observed $\lambda = 1.3$ mm continuum image. IRS 3A and 3B are distinct, but IRS 3C is marginally detected. The vectors in Figure 1 indicate the linear polarization direction, which will be discussed in §7. The locations of IRS 3A, 3B, and 3C in Figure 1 are from Looney et al. (2000). Table 1 summarizes locations, fluxes, and estimated masses of the three sources. To estimate the mass of the circumstellar material (envelopes and disks), we assume optically thin dust emission and a uniform envelope dust temperature of 35 K,

$$F_\nu = B_\nu(T_{dust}) \kappa_\nu M_{tot} D^{-2} \quad (1)$$

where B_ν is a black-body intensity of a temperature T_{dust} , κ_ν is a mass absorption coefficient, M_{tot} is the total mass of gas and dust, and D is the source distance. We assume a mass absorption coefficient, $\kappa_\nu = 0.005 \text{ cm}^2 \text{ g}^{-1}$ at $\lambda = 1.3$ mm. The mass absorption coefficient was acquired following a dust emissivity model of a power law ($\kappa_\nu \sim \lambda^{-\beta}$) with $\beta = 1$. Dust emissivity studies of submillimeter wavelengths suggested λ^{-1} dependence in circumstellar disks and dense cores rather than λ^{-2} (Weintraub et al. 1989; Beckwith et al. 1990; Beckwith & Sargent 1991; Looney et al. 2003).

4. ^{13}CO $J = 1 \rightarrow 0$ and C^{18}O $J = 1 \rightarrow 0$ observation

We detect all three sources (IRS 3A, 3B, and 3C) in ^{13}CO and C^{18}O . Figures 2 and 3 show the ^{13}CO $J = 1 \rightarrow 0$ and C^{18}O $J = 1 \rightarrow 0$ channel maps, respectively. IRS 3C peaks are in the 3.8 km s^{-1} channel of ^{13}CO and 3.7 km s^{-1} channel of C^{18}O . The emission from IRS 3A and 3B is distributed over different velocity channels; IRS 3A is around the 5 and 6 km s^{-1} channels in the two spectral lines, while IRS 3B is around the 4 and 5 km s^{-1} channels. This implies that the envelopes of IRS 3A and 3B have a velocity difference less than 1 km s^{-1} . Terebey & Padgett (1997) have reported a velocity-position diagram of C^{18}O $J = 1 \rightarrow 0$ with a comparable angular and spectral resolution to ours, showing these velocity differences between IRS 3A, 3B, and 3C. They suggested kinematics of the binary system IRS 3A and 3B, as well as a rotating system consisting of IRS 3C and the common envelope of IRS 3A and 3B. However, they did not discuss the physical conditions of the presumed binary system. We discuss the binary system of IRS 3A and 3B in §6, based on their velocity difference and the two outflows shown in the following section. Moreover, we estimate the specific angular momentum of the binary system.

Isotopic observations such as ^{13}CO and C^{18}O are used to trace denser regions and to verify their optical depth. However, we do not follow the standard procedure because the masses of envelopes are better estimated using our dust emission data, especially in the case of complicated regions like IRS 3. Also, these isotopes may not trace outflows. Instead, we use the optical depth results of Bachiller et al. (1990), deduced from CO $J = 1 \rightarrow 0$ and CO $J = 2 \rightarrow 1$, and follow their procedures to estimate the outflow masses in §5.2.

5. CO $J = 2 \rightarrow 1$ observation

5.1. Bipolar Outflows

As introduced in §1, one, two, or up to three outflows have been suggested for this region. Bachiller et al. (1990) proposed that an outflow in the east-west direction originates from IRS 3, based on a redshifted component that was detected in the region of the blueshifted lobe of the mm source outflow. Recently Wolf-Chase et al. (2000) suggested outflows of position angle 150° and 129° from IRS 3A and 3B respectively, using their large-scale CO $J = 1 \rightarrow 0$ observation as well as previous studies of H_2 observations and Herbig-Haro objects. In addition, Girart & Acord (2001) presented a redshifted SiO component along a line of position angle of 110° from IRS 3B. However, to date there were no observations with enough angular resolution to clearly identify outflows with sources. Here we present high angular resolution BIMA observations to illustrate outflows in IRS 3. We reveal two outflows

from IRS 3A and 3B but no outflow from IRS 3C, based on channel maps and integrated intensity maps.

Figure 4 shows the CO $J = 2 \rightarrow 1$ channel maps with a velocity range from +29 to -36 km s^{-1} . The values in the upper left of each panel indicate the channel central velocities in units of km s^{-1} and the two lines in each panel show our determined directions of the two outflows originating from IRS 3A and 3B. As introduced in §4, the V_{LSR} of these sources is around 5 km s^{-1} , which is located at the boundary between the $+7$ and $+3 \text{ km s}^{-1}$ channels.

The outflow of IRS 3A is mainly shown in two channels around V_{LSR} , $+7$ and $+3 \text{ km s}^{-1}$ channels, with symmetric features cross the central source. Some redshifted components of the IRS 3A outflow also appear in the $+15$ and $+11 \text{ km s}^{-1}$ channels. The feature might be just an elongated cloud. However, the ^{13}CO and C^{18}O maps indicating ambient clouds do not show such features. In addition, the facts that two channels of $+7$ and $+3 \text{ km s}^{-1}$ show a very similar shape to each other, that two redshifted channels of $+15$ and $+11 \text{ km s}^{-1}$ have blobs on both sides of IRS 3A, and that H_2 emission observations reveal a string of H_2 knots in a consistent direction (Davis & Smith 1995; Eislöffel 2000), strongly suggest that it is an outflow nearly perpendicular to the line of sight, originating from IRS 3A. The position angle of the IRS 3A outflow is 155° .

As shown in Figure 4, the outflow from IRS 3B appears from the $+23 \text{ km s}^{-1}$ channel, an end channel of a redshifted lobe, along the position angle of 105° . This position angle is consistent with the Girart & Acord (2001) estimate of 110° . The redshifted lobe is clearly seen from the $+23$ to $+11 \text{ km s}^{-1}$ channels and overlaps with the southern lobe originating from IRS 3A in the $+7$ and $+3 \text{ km s}^{-1}$ channels. Note that the blueshifted channels after $+3 \text{ km s}^{-1}$ look complicated with many blobs. This can be explained by the overlap with the blueshifted lobe of the mm source outflow, located $70''$ southeast. Indeed, the velocity range of the mm source's blueshifted outflow lobe is consistent with these channels (see Fig.10 in Bachiller et al. 1990). Due to the complexity in blueshifted channels, the outflow direction is deduced from the redshifted channels first. However, we can still see the blueshifted components of the IRS 3B outflow up to -30 km s^{-1} along the 105° position angle. In addition, a string of three blobs along the outflow direction is shown in the -5.2 km s^{-1} channel. The blobs in the $+15$ and $+11 \text{ km s}^{-1}$ channels can be the opposite components of these three blobs.

Figure 5 is an integrated intensity map of CO $J = 2 \rightarrow 1$ that more clearly shows the outflows. The red contours present a velocity range from $+25$ to $+9 \text{ km s}^{-1}$, black contours from $+9$ to $+1 \text{ km s}^{-1}$, and blue contours from $+1$ to -32 km s^{-1} . Again, the blue contours appear with several blobs due to the effect of the overlapped blueshifted lobe of the mm source outflow. This integrated intensity map confirms two outflows originating from IRS

3A and 3B as suggested from channel maps. Black contours in Figure 5 show an outflow from IRS 3A and especially the redshifted and blueshifted lobes around IRS 3B are clearly seen.

5.2. Mass, Momentum, and Energy

Bachiller et al. (1990) showed that the outflow regions in IRS 3 are optically thin in CO, using CO $J = 2 \rightarrow 1$ and $J = 1 \rightarrow 0$ lines instead of the CO isotopes ^{13}CO or C^{18}O , since the outflow regions are not dense enough to be traced by these isotopic observations. In addition, they estimated the excitation temperature of CO. As described in Bachiller et al. (1990), the CO column density can be estimated from the integrated intensity, assuming optically thin emission and level populations in local thermal equilibrium at the excitation temperature T_{21} ,

$$\frac{N(\text{CO})}{\text{cm}^{-2}} = 1.06 \times 10^{13} T_{21} \exp(16.5/T_{21}) \int T_R(2-1) d\left(\frac{v}{\text{km s}^{-1}}\right). \quad (2)$$

To estimate the masses of the lobes, we assume a typical abundance of CO, $\text{CO}/\text{H}_2 = x(\text{CO}) \sim 10^{-4}$, optically thin CO emission in outflow regions, and a CO excitation temperature of 11 K, as reported by Bachiller et al. (1990). These assumptions give the mass estimate equation,

$$\begin{aligned} M_{lobe} &= 2m_H A_{lobe} 10^4 N(\text{CO}) \\ &= 2m_H 5.23 \times 10^{-5} \frac{\lambda^2 D^2}{2k} \int \frac{F_{lobe}(\text{CO } 2-1)}{Jy} d\left(\frac{v}{\text{km s}^{-1}}\right) \\ &= 3.22 \times 10^{-6} \text{ M}_\odot \left(\frac{D}{250 \text{ pc}}\right)^2 \int \frac{F_{lobe}(\text{CO } 2-1)}{Jy} d\left(\frac{v}{\text{km s}^{-1}}\right) \end{aligned} \quad (3)$$

where $A_{lobe} = \Omega D^2$ is the lobe area and F_{lobe} is the total lobe flux density. The mass estimates are summarized in Table 2 with momentum and kinetic energy. Note that the errors tabulated are only statistical errors. Moreover, important uncertainties like CO opacities and unknown 3-D geometry of outflows affect these outflow mass estimates (Lada 1985; Bachiller et al. 1990). In the case of the blueshifted lobes, there is also the uncertainty from the contribution of the mm source outflow.

We also need to consider that interferometric observations resolve out flux from extended structures. The missing flux makes mass estimates of extended structures difficult and underestimated. On the other hand, interferometry is a powerful technique that can reveal small structures overlapped with large-scale emission. In this case, L1448 IRS 3 is overlapped with the large blueshifted lobe of the L1448-mm outflow. Therefore, we have the advantage

of minimizing the L1448-mm outflow contamination as well as the disadvantage of losing the flux of extended features. The uv coverage of our observations allows us to recover flux up to $15''$ structures. The missing flux is less significant in elongated structures because it also depends on the size-scales of the minor axis.

Compared to the single dish observations (beam size $\sim 12''$) of Bachiller et al. (1990), there is no significant missing flux in the redshifted wing ($\gtrsim 10 \text{ km s}^{-1}$); the flux is consistent within the uncertainties. The low velocity components (0 to 10 km s^{-1}) are dominated by the ambient cloud (Bachiller et al. 1990). Since our two channels in that velocity range still show outflow features consistent with the redshifted channels (see Fig. 4), we argue that the majority of missing flux comes from the ambient cloud emission. From this point of view, the missing flux is a large advantage as it avoids contamination with the ambient cloud emission rather than the disadvantage of losing flux. On the other hand, the channel with -1.1 km s^{-1} central velocity may experience relatively large flux loss, as the IRS 3B outflow feature disappears or is indistinct from the extended, and mostly resolved-out, blueshifted lobe of the L1448-mm source. The missing flux in this channel would cause an underestimation of the IRS 3B outflow mass but does not significantly affect our interpretations. We discuss the effects caused by the missing flux in this channel later in related sections. Overall, although the true size of the emission is unknown, we conclude that the missing flux probably does not significantly affect our results.

We estimate the masses of the northern and the southern lobes of the IRS 3A outflow as 0.70×10^{-3} and $1.12 \times 10^{-3} M_{\odot}$, respectively. Considering that the southern lobe is overlapped with a portion of a redshifted lobe of an outflow from IRS 3B, we can regard $0.42 \times 10^{-3} M_{\odot}$ (the mass difference of the two lobes) as coming from IRS 3B. This assumes that the two lobes from an outflow have similar masses. As a result, the northern and the southern lobes of IRS 3A outflow have $\sim 0.70 \times 10^{-3} M_{\odot}$ each.

The redshifted and blueshifted lobes of the outflow originating from IRS 3B are well distinguished in the velocity range $+25$ to -32 km s^{-1} . The outflow spans the blue, black, and red contours in Figure 5. The blueshifted lobe of this outflow has $0.98 \times 10^{-3} M_{\odot}$, which is comparable to the $0.75 \times 10^{-3} M_{\odot}$ of the redshifted lobe as a combination of the red contours ($0.33 \times 10^{-3} M_{\odot}$) and a portion of the black contours ($0.42 \times 10^{-3} M_{\odot}$). The difference is reasonable, considering the blueshifted regions are contaminated by components of the mm source outflow, probable flux loss in the -1.1 km s^{-1} channel, and flux gain in other blueshifted channels. In summary, the redshifted lobe of the IRS 3B outflow has $0.75 \times 10^{-3} M_{\odot}$ and the blueshifted lobe has $0.98 \times 10^{-3} M_{\odot}$, comparable within the uncertainties.

Estimates of momentum and kinetic energy of each component are also shown in Table 2. We use $V_{LSR} = 5 \text{ km s}^{-1}$ and do not apply the inclination factors, which are $1/\cos\theta$ for

momentum and $1/\cos^2\theta$ for kinetic energy. Here θ is the inclination angle from the line of sight. When calculating the momentum and kinetic energy, we assume that components in each channel have the central channel velocity. Comparing momentum and energy of each lobe of the two outflows, the southern lobe of the IRS 3A outflow and the eastern lobe of the IRS 3B outflow have lower momentum and kinetic energy than their opposite lobes. Although the contamination of the L1448-mm outflow in the blueshifted lobe of the IRS 3B outflow and the nearly perpendicular aspect of the IRS 3A outflow to the line of sight make the interpretation difficult, it is probable that the outflows from IRS 3A and 3B interact in the overlapped region because the kinetic energy difference is distinct even when considering a portion of the blueshifted lobe of IRS 3B to be the same mass as the redshifted lobe. Due to the collision of two outflows, the kinetic energy would be reduced. The fact that there is no blueshifted opponent of the small redshifted blobs of the IRS 3A outflow in the $+15 \text{ km s}^{-1}$ channel supports this idea as well. Besides, the heated clump, which Curiel et al. (1999) presented near IRS 3 in observations of the NH_3 (J, K) = (1, 1) and (2, 2) inversion transitions, is located in the overlapped region of the two outflows from IRS 3A and 3B. Although they argued that the heated clump would be a part of a larger heated region because IRS 3 is at the edge of their field, it may present the interaction of the two outflows. In addition, the fact that the redshifted component of the IRS 3B outflow detected in SiO $J = 2 \rightarrow 1$ over the interaction region has relatively low velocity compared to the blueshifted component (Girart & Acord 2001), also supports interaction. Based on these considerations, we also suggest that IRS 3B is closer than IRS 3A because this deployment can reproduce the interaction. This is pointed out again later, in the CO $J = 2 \rightarrow 1$ linear polarization of §7.

5.3. Velocity, Inclination, and Opening

Based on the mass of the outflow lobes and an assumed mass loss rate, we can check whether or not the IRS 3A outflow is nearly perpendicular. If we assume a mass loss rate of $6 \times 10^{-7} \text{ M}_\odot \text{ yr}^{-1}$ from the two outflow lobes², the age of the outflow would be ~ 2300 years and the proper velocity of the outflow would be $\sim 10 \text{ km s}^{-1}$ since the outflows extend to $20''$ (5000 AU at 250 pc). As the channel width is 4 km s^{-1} and the V_{LSR} is on the boundary of the two channels showing the outflow feature, the inclination including opening angle must

²This is consistent with previous studies suggesting that massive young stars lose mass up to $10^{-3} \text{ M}_\odot \text{ yr}^{-1}$ and low mass stars down to $10^{-9} \text{ M}_\odot \text{ yr}^{-1}$ (e.g. Kim & Kurtz 2006; Wu et al. 2004; Bontemps et al. 1996). In order to obtain a reasonable outflow velocity ($\sim 10 \text{ km s}^{-1}$), we assume a mass loss rate of $6 \times 10^{-7} \text{ M}_\odot \text{ yr}^{-1}$.

be less than 22° from the plane of the sky; the IRS 3A outflow is nearly perpendicular to the line of sight.

The inclination angle of IRS 3B can be estimated from the velocity features detected. Figure 6 presents a velocity-position diagram cut along the outflow direction of position angle 105° from IRS 3B. Both redshifted (east) and blueshifted (west) lobes are divided into two components: one accelerating from the source and the other with a constant velocity. Using Figures 6 and 4, the accelerating portion up to $+23 \text{ km s}^{-1}$ (channel central velocity) and the constant part at $+3 \text{ km s}^{-1}$ are in the eastern (redshifted) region. Similarly, the accelerating portion up to -30 km s^{-1} and the constant part at -5 km s^{-1} are in the western (blueshifted) region. These velocities are $+18, -2, -10$, and -35 km s^{-1} in the IRS 3B rest frame ($V_{LSR} = +5 \text{ km s}^{-1}$). If the missing flux in the -1.1 km s^{-1} channel is part of the constant component, then arguable -6 km s^{-1} in the IRS 3B rest frame is a better extreme constant velocity. However, since the small difference in velocity will not significantly change the results derived below and since it is strongly dependent on the assumed missing flux, we use -10 km s^{-1} in the IRS 3B rest frame as the velocity of the constant velocity component in blueshifted region.

The constant and accelerating features are best explained by two possible geometric outflow effects, although an outflow with various velocity components is also a possible explanation. One is the geometric effect caused by precession and the other by a trumpet-shaped outflow. The precession of the IRS 3B outflow— the side of the redshifted lobe is precessing toward the observer and the side of the blueshifted lobe is away from the observer, would give the detected map features. In other words, the redshifted or blueshifted components further from the central source are older components emitted when the inclination was smaller than now. Therefore, the outflow is observed as accelerating away from the source, even assuming a constant outflow velocity. A trumpet-shaped outflow can also give the detected features. The “trumpet” outflow has different angles with respect to the line of sight along the redshifted or blueshifted lobes. These different angles can give the accelerating feature depending on the outflow inclination.

The nice aspect of the “trumpet” outflow is that we can estimate outflow parameters such as velocity, inclination angle, and opening angle, based on the observed data. The opening angle is assumed as the angle on the end of the outflow “trumpet”. Therefore, the velocity difference between accelerating and non-accelerating features of the redshifted or blueshifted lobe is coming from the opening angle. In addition to the velocity (v), the inclination angle (θ_i), and the opening angle (θ_o), we adopt the velocity difference (Δv) and the opening angle difference ($\Delta\theta_o$) between the redshifted and blueshifted lobes. Note that the inclination angle is measured from the line of sight and that the opening angle is half of

the outflow opening. As mentioned in the previous section, since the redshifted lobe of the IRS 3B outflow is likely to be interacting with the southern lobe of the IRS 3A outflow, a velocity difference needs to be included. The reason for applying the opening angle difference is that the side of the redshifted lobe has components in a blueshifted channel with a central velocity of $+3 \text{ km s}^{-1}$ (Fig. 4), while the side of the blueshifted lobe does not. We define the velocity difference as $\Delta v = v_{blue} - v_{red} > 0$ ($v = v_{blue}$) and the opening angle difference as $\Delta\theta_o = \theta_{o,red} - \theta_{o,blue} > 0$ ($\theta_o = \theta_{o,blue}$). The blueshifted lobe is expected to have a higher velocity and a narrower opening angle than the redshifted lobe. Using Bayesian statistics, we determine the most likely parameter combinations to explain the observed velocity features,

$$P(\{\text{parameters}\} | \{v'_i\}) = \frac{P(\{v'_i\} | \{\text{parameters}\})}{P(\{v'_i\})} P(\{\text{parameters}\}),$$

where $\{\text{parameters}\} = \{v, \theta_i, \theta_o, \Delta v, \Delta\theta_o\}$. (4)

The $\{v'_i\}$ is a set of four extreme values of the observed line-of-sight velocities in the outflow lobes with respect to the IRS 3B rest frame (v_1, v_2, v_3 , and v_4), so the evidence term, $P(\{v'_i\}) = 1$. In addition, since we do not have any preference to choose the five parameters, we assume that the prior probability densities, $P(\{\text{parameters}\})$, are uniform. However, note that the opening angle should be less than 45° ; otherwise, we would observe redshifted components on the side of the blueshifted lobe as well as the blueshifted components on the side of the redshifted lobe. For the likelihood, $P(\{v'_i\} | \{\text{parameters}\})$, we choose a probability density having a constant value in the channel width (4 km s^{-1}) and exponentially decreasing outside of the channel width.

We found the parameters giving the maximum posterior probability, after taking into account central velocities of four-end channels showing outflow features in the IRS 3B rest frame, $\{v'_i\} = \{+18, -2, -10, -35\} \text{ km s}^{-1}$. The maximum posterior is obtained when the four velocities estimated from the five parameters are in the flat-top regions of each channel. Note that we adopted the likelihood (indicating channels) of functions having a constant value (flat-top) in the channel width (4 km s^{-1}) and exponentially decreasing outside. To explore the parameter space, the Metropolis-Hastings method (MacKay 2003) was used; we obtained a few hundred thousand samples with the maximum posterior probability through one million trials. Since we use flat-top shaped channel functions for the likelihood, the parameters are largely distributed. For example, the velocity distribution peaks at around 40 km s^{-1} and quickly drops, but some cases have even a few hundred km s^{-1} . The inclination angle and the opening angle are distributed in $30 \sim 80^\circ$ and $5 \sim 45^\circ$, respectively.

However, as these parameters are not independent of each other, we can narrow the acceptable range of parameters. Figure 7 shows the velocity (solid circles), the inclination angle (solid squares), and the velocity and opening angle differences (open circles and open

triangles, respectively) versus the opening angle. The opening angle is also plotted (solid triangles) to compare with the other parameters. For the plot, samples are divided by 5° bins of the opening angle and each bin has a few tens of thousand samples. The data points in Figure 7 are average values of the samples in each bin, and the error bars present their standard deviation. The dotted line without data points indicates the opening angle plus the opening angle difference, in other words, the redshifted opening angle. Note that small opening angles with relatively large velocities and inclination angles or large opening angles with small velocities and inclination angles give the four observed line-of-sight velocities. However, opening angles larger than 26° are rejected because they have the 18 km s^{−1} component with the −10 km s^{−1} component on the same side, which is not consistent with our observation (Fig. 6). Too small opening angles (< 8°) are also not likely due to the too large velocities required. As a result, we can constrain the opening angle to 8° < θ_o < 26° and the other parameters to the values following the opening angle; for examples, 100 \gtrsim v \gtrsim 40 km s^{−1} and 75° \gtrsim θ_i \gtrsim 50°. Recent Spitzer Space Telescope (SST) observations have suggested that an opening angle of \sim 20° is preferred (Tobin et al. in preparation). In that case, we constrain the inclination angle to \sim 57°, which is consistent with the SST observational results within uncertainties, and the velocity to \sim 45 km s^{−1}. These parameters give the age of the IRS 3B outflow detected in our field-of-view as \sim 600 years.

6. Binary system of IRS 3A and 3B

The velocity difference between IRS 3A and 3B detected in the ¹³CO $J = 1 \rightarrow 0$ and C¹⁸O $J = 1 \rightarrow 0$ observations can be understood as an orbiting binary system. This also supports the interaction of the two outflows from IRS 3A and 3B. Here we introduce a kinematical constraint for a Class 0 binary system.

When denominating velocities of the two clouds with respect to the center of mass of the binary system as v_A (> 0) and v_B (< 0) and the components of the velocities in the line-of-sight plane of the IRS 3A and 3B as v_{A||} and v_{B||}, the projected velocities on the line of sight are v'_A = v_{A||}sinθ and v'_B = v_{B||}sinθ (Fig. 8). Note that the vertical velocity components to the plane are v_{A⊥} and v_{B⊥}, and so the proper motion velocities are indicated as (v_{A||}²cos²θ + v_{A⊥}²)^{1/2} and (v_{B||}²cos²θ + v_{B⊥}²)^{1/2}. Similarly, the projected semimajor axis is a' = asinθ \approx 7" \times 250 pc = 1750 AU. These projected velocity difference (here assuming 0.8 km s^{−1}) and the projected semimajor axis (\sim 1750 AU) allow the estimation of the orbiting period (P) of the binary system,

$$|v_A| = \sqrt{v_{A||}^2 + v_{A\perp}^2} = \frac{2\pi a_A}{P} > |v_{A||}|$$

$$|v_B| = \sqrt{v_{B\parallel}^2 + v_{B\perp}^2} = \frac{2\pi a_B}{P} > |v_{B\parallel}|.$$

Multiplying by $\sin\theta$, they become

$$\begin{aligned} |v_{A\parallel}| \sin\theta &< \frac{2\pi a_A \sin\theta}{P} \\ |v_{B\parallel}| \sin\theta &< \frac{2\pi a_B \sin\theta}{P} \end{aligned}$$

and adding each side gives

$$|v'_A| + |v'_B| < \frac{2\pi a'}{P}. \quad (5)$$

In equation (5), since v'_B is negative, the left hand side is the projected velocity difference, 0.8 km s^{-1} . Using the projected semimajor axis (1750 AU), we obtain an upper limit of the orbiting period, $\sim 6.54 \times 10^4$ years. Note that it is much longer than the age (~ 2300 years) of the IRS 3A outflow, which is obtained assuming the mass loss rate, and the estimated age (~ 600 years) of the IRS 3B outflow. Furthermore, since the masses of the two clouds were estimated as 0.21 and $1.15 M_\odot$ in §3 and Table 1, we can also estimate an upper limit of the semimajor axis from the Kepler's third law,

$$\frac{a}{AU} = \left(\left(\frac{m_A + m_B}{M_\odot} \right) \left(\frac{P}{\text{yr}} \right)^2 \right)^{1/3}. \quad (6)$$

The estimated masses and the orbiting period give a semimajor axis of ~ 1800 AU, a slightly larger value than the projected semimajor axis. In this case, the $\theta = \sin^{-1}(a'/a)$ is about 76° (refer to Fig. 8), which means that the considered velocity difference (0.8 km s^{-1}) is acceptable for a gravitationally bound binary system. Note that the unconsidered central luminous sources can increase the semimajor axis by 26% ($= 2^{1/3}$) when they are assumed to have identical masses to the circumstellar material. This increases the probability of a gravitationally bound binary system. If the velocity difference were estimated as 0.5 km s^{-1} from higher spectral resolution observations, the upper limit of the orbiting period would be 1.05×10^5 years, the semimajor axis would be 2500 AU, and the $\theta = \sin^{-1}(a'/a)$ would be 44° . As described above, the total mass and the projected velocity difference and semimajor axis give a kinematical, gravitationally bound constraint on apparent binary systems. Since the projected velocity difference is within values for a binary system, we conclude that the IRS 3A and 3B sources are likely to be gravitationally bound. Observations with higher spectral resolution will give a better constraint.

The angular momentum of the binary system is also noteworthy. We estimate the specific angular momentum (angular momentum per unit mass) of this binary system using the projected velocity components, the projected distance, and the mass ratio from the mass

estimates of the continuum emission at $\lambda = 1.3$ mm. This estimate has uncertainties caused by the ambiguities of velocities of the line of sight as well as proper motions. The ambiguity of the line of sight comes from the broad channel width of our observation. If we can remove the ambiguity using higher spectral resolution observation, the estimate would be a lower limit of the specific angular momentum. The value is $\sim 3 \times 10^{20} \text{ cm}^2 \text{ s}^{-1}$, similar to the upper limit of the specific angular momentum of binaries and to the lower limit of molecular clouds in Taurus (Simon et al. 1995; Goodman et al. 1993).

7. Magnetic Fields

Linear polarization is marginally detected in both the $\lambda = 1.3$ mm continuum and CO $J = 2 \rightarrow 1$ spectral line. Vectors around IRS 3B in Figure 1 present polarization detected in the $\lambda = 1.3$ mm continuum. Since polarization of dust emission is perpendicular to the magnetic field, the magnetic field is expected in the north-south direction around IRS 3B. This is consistent with the large scale magnetic field observed by SCUBA at $\lambda = 850 \mu\text{m}$ shown in Figure 9. Note that the vectors in Figure 9 also indicate linear polarization and the direction around IRS 3B is east-west like the $\lambda = 1.3$ mm continuum data in Figure 1. Toward the center of IRS 3B, weaker linear polarization is detected at both wavelengths. The polarization fractions are around 5% in our BIMA 1.3 mm continuum and around 2% in the SCUBA data. This smaller polarization fraction of the SCUBA data is from the larger beam size of SCUBA smearing out the linear polarization.

Linear polarization of the CO $J = 2 \rightarrow 1$ emission, tracing the outflows, was detected in patches of the overlapped region of the southern lobe of the IRS 3A outflow and the redshifted lobe of the IRS 3B outflow. Figure 10 is an intensity map of two channels combined in velocity from $+1$ to $+9 \text{ km s}^{-1}$. Vectors present linear polarization directions and two lines on IRS 3A and 3B indicate outflow directions. According to the Goldreich-Kylafis effect (e.g. Kylafis 1983), linear polarization of spectral lines can be either parallel or perpendicular to magnetic field, depending on the relation between line of sight, magnetic field direction, and velocity gradient. Since the polarization was detected in only a few small patches located in the overlapped region of the IRS 3A and 3B outflows, it is hard to define the morphology of the magnetic fields. However, as the vectors are likely parallel or perpendicular to the IRS 3B outflow, we suggest that the polarization comes from the IRS 3B outflow. At the same time, this suggestion implies that the magnetic field may be perpendicular or parallel to the outflow³. Although we cannot distinguish between the two, the parallel magnetic field can

³Girart et al. (1999) detected CO $J = 2 \rightarrow 1$ polarization perpendicular to dust polarization in NGC

be from a large scale magnetic field morphology (hour glass morphology) widely accepted in forming protostars, and the perpendicular magnetic field can be from a helical structure extended from a toroidal magnetic field suggested by some theories (e.g. Ostriker 1997). The fraction of linear polarization is around 6 to 15%.

Based on both dust polarization and CO $J = 2 \rightarrow 1$ polarization, we suggest a unified magnetic field morphology related to the disk and outflow structures in forming protostars. The magnetic field inferred from the dust emission, perpendicular to outflow, may show a toroidal magnetic field around a circumstellar disk and the magnetic field inferred from CO $J = 2 \rightarrow 1$ may present a large scale morphology parallel to the outflow or helical structure perpendicular to the outflow. As discussed in §5, we can also suggest that the IRS 3B source is closer, because the polarization appears to be from IRS 3B. Polarization of the farther source (IRS 3A) is harder to detect due to the foreground cloud (IRS 3B).

8. Summary and Discussion

We present CO $J = 2 \rightarrow 1$, $^{13}\text{CO } J = 1 \rightarrow 0$ and $\text{C}^{18}\text{O } J = 1 \rightarrow 0$ observations, and $\lambda = 1.3$ mm continuum and CO $J = 2 \rightarrow 1$ polarimetric observations. IRS 3A and 3B are distinctly detected with mass estimates of 0.21 and $1.15 M_{\odot}$ respectively at $\lambda = 1.3$ mm, but IRS 3C is marginally detected with upper mass limit of $0.03 M_{\odot}$ (§3). The ambient velocities of IRS 3A, 3B, and 3C are estimated as 5.5, 4.5, and 3.5 km s^{-1} , respectively, from $^{13}\text{CO } J = 1 \rightarrow 0$ and $\text{C}^{18}\text{O } J = 1 \rightarrow 0$ channel maps (§4). The two close sources, IRS 3A and 3B, have a velocity difference less than 1 km s^{-1} ; the difference is a kinematical constraint on a gravitationally bound binary system. Moreover, we estimated the specific angular momentum of the binary system as $\sim 3 \times 10^{20} \text{ cm}^2 \text{ s}^{-1}$, similar to the upper limit of binaries and to the lower limit of molecular clouds in Taurus (§6).

We present CO $J = 2 \rightarrow 1$ observations showing two outflows, one each from IRS 3A and 3B (§5). The outflow driven by IRS 3A has PA = 155° and is nearly perpendicular to the line of sight, while the outflow by IRS 3B has PA = 105° . In addition, we posit that the two outflows are interacting in the southern lobe of the IRS 3A outflow and the redshifted

1333 IRAS 4A and interpreted the spectral line polarization as parallel to the magnetic field. However, polarization in dust continuum and CO $J = 2 \rightarrow 1$ may not indicate the same magnetic field because dust continuum and CO $J = 2 \rightarrow 1$ trace different density regions; the magnetic field direction at the central core may change radially from an hour glass morphology (e.g. Fiedler & Mouschovias 1993). In addition, detected polarization directions in our dust emission and CO $J = 2 \rightarrow 1$ data are likely to be parallel around the IRS 3B center. Therefore, we cannot define the magnetic field direction as either perpendicular or parallel to the CO $J = 2 \rightarrow 1$ polarization here.

lobe of the IRS 3B outflow, based on a comparison of the kinetic energies of lobes. Coupled with the fact that the linear polarization detected in CO $J = 2 \rightarrow 1$ is likely to come from the IRS 3B outflow, IRS 3B is closer than IRS 3A. We also detected that the IRS 3B outflow has accelerating and non-accelerating features in the velocity-position diagram, which is interpreted as either a precessing outflow or a “trumpet” outflow. Assuming a “trumpet” outflow of IRS 3B rather than its precession, we estimated the velocity, inclination angle, and the opening angle, using Bayesian statistics. The velocity and the inclination angle are constrained between 100 and 40 km s⁻¹ and between 75° and 50°, respectively, as the opening angle between 8° and 26°. Furthermore, using an opening angle of $\sim 20^\circ$ from Spitzer Space Telescope observations, the velocity and the inclination angle of the IRS 3B outflow are ~ 45 km s⁻¹ and $\sim 57^\circ$.

Linear polarization in both the $\lambda = 1.3$ mm continuum and CO $J = 2 \rightarrow 1$ spectral line is marginally detected around the center and outflow of IRS 3B, respectively (§7). The dust emission polarization gives a magnetic field perpendicular to the outflow, which may be a toroidal magnetic field parallel to the circumstellar disk. In contrast, the spectral line polarization suggests either a perpendicular or a parallel magnetic field to the IRS 3B outflow. To determine the relation between the magnetic field and the outflow direction, more sensitive polarimetric observations are required.

The L1448 IRS 3 is an excellent region to study star formation. The IRS 3A outflow, nearly perpendicular to the line of sight, enables the study of the disk and outflow structures in protostellar systems more easily, since it shows the profile projected in the plane of the sky. In addition, the binary system of IRS 3A and 3B having two outflows in quite different directions gives an opportunity to study the interaction between two sources as well as constrain binary system formation itself. Finally, more sensitive polarimetric observations will provide clues on the connection between outflows and magnetic fields.

The authors acknowledge support from the Laboratory for Astronomical Imaging at the University of Illinois and NSF AST 0228953. W. K. thanks Ben Wandelt for discussions on Bayesian statistics and an anonymous referee for helpful comments. The JCMT Archive project is a collaboration between the Canadian Astronomy Data Centre (CADC), Victoria and the James Clerk Maxwell Telescope (JCMT), Hilo. Funding for the CADC’s JCMT Archive effort is provided by the National Research Council of Canada’s (NRC) to the Herzberg Institute of Astrophysics.

Facilities: BIMA, JCMT (SCUBA)

REFERENCES

Archibald, E. N., Dunlop, J. S., Jimenez, R., Friaça, A. C. S., McLure, R. J., & Hughes, D. H. 2002, MNRAS, 336, 353

Bachiller, R. & Cernicharo, J. 1986, A&A, 168, 262

Bachiller, R., Guilloteau, S., Dutrey, A., Planesas, P., & Martin-Pintado, J. 1995, A&A, 299, 857

Bachiller, R., Martin-Pintado, J., Tafalla, M., Cernicharo, J., & Lazareff, B. 1990, A&A, 231, 174

Bally, J., Devine, D., Alten, V., & Sutherland, R. S. 1997, ApJ, 478, 603

Barsony, M., Ward-Thompson, D., André, P., & O'Linger, J. 1998, ApJ, 509, 733

Beckwith, S. V. W. & Sargent, A. I. 1991, ApJ, 381, 250

Beckwith, S. V. W., Sargent, A. I., Chini, R. S., & Guesten, R. 1990, AJ, 99, 924

Bontemps, S., Andre, P., Terebey, S., & Cabrit, S. 1996, A&A, 311, 858

Chandrasekhar, S. & Fermi, E. 1953, ApJ, 118, 113

Ciardi, D. R., Telesco, C. M., Williams, J. P., Fisher, R. S., Packham, C., Piña, R., & Radomski, J. 2003, ApJ, 585, 392

Crutcher, R. M. 1999, ApJ, 520, 706

Crutcher, R. M., Nutter, D. J., Ward-Thompson, D., & Kirk, J. M. 2004, ApJ, 600, 279

Curiel, S., Raymond, J. C., Moran, J. M., Rodriguez, L. F., & Canto, J. 1990, ApJ, 365, L85

Curiel, S., Torrelles, J. M., Rodríguez, L. F., Gómez, J. F., & Anglada, G. 1999, ApJ, 527, 310

Davis, C. J. & Smith, M. D. 1995, ApJ, 443, L41

Eislöffel, J. 2000, A&A, 354, 236

Enoch, M. L., Young, K. E., Glenn, J., Evans, II, N. J., Golwala, S., Sargent, A. I., Harvey, P., Aguirre, J., Goldin, A., Haig, D., Huard, T. L., Lange, A., Laurent, G., Maloney, P., Mauskopf, P., Rossinot, P., & Sayers, J. 2006, ApJ, 638, 293

Fiedler, R. A. & Mouschovias, T. C. 1993, *ApJ*, 415, 680

Girart, J. M. & Acord, J. M. P. 2001, *ApJ*, 552, L63

Girart, J. M., Crutcher, R. M., & Rao, R. 1999, *ApJ*, 525, L109

Goodman, A. A., Benson, P. J., Fuller, G. A., & Myers, P. C. 1993, *ApJ*, 406, 528

Greaves, J. S., Holland, W. S., Jenness, T., Chrysostomou, A., Berry, D. S., Murray, A. G., Tamura, M., Robson, E. I., Ade, P. A. R., Nartallo, R., Stevens, J. A., Momose, M., Morino, J.-I., Moriarty-Schieven, G., Gannaway, F., & Haynes, C. V. 2003, *MNRAS*, 340, 353

Hatchell, J., Richer, J. S., Fuller, G. A., Qualtrough, C. J., Ladd, E. F., & Chandler, C. J. 2005, *A&A*, 440, 151

Holland, W. S., Robson, E. I., Gear, W. K., Cunningham, C. R., Lightfoot, J. F., Jenness, T., Ivison, R. J., Stevens, J. A., Ade, P. A. R., Griffin, M. J., Duncan, W. D., Murphy, J. A., & Naylor, D. A. 1999, *MNRAS*, 303, 659

Kim, K.-T. & Kurtz, S. E. 2006, *ApJ*, 643, 978

Kylafis, N. D. 1983, *ApJ*, 275, 135

Lada, C. J. 1985, *ARA&A*, 23, 267

Looney, L. W., Mundy, L. G., & Welch, W. J. 2000, *ApJ*, 529, 477

—. 2003, *ApJ*, 592, 255

MacKay, D. J. C. 2003, *Information Theory, Inference, and Learning Algorithms* (Cambridge, UK: Cambridge University Press)

Ostriker, E. C. 1997, *ApJ*, 486, 291

Rao, R., Crutcher, R. M., Plambeck, R. L., & Wright, M. C. H. 1998, *ApJ*, 502, L75

Rao, R. P. 1999, Ph.D. Thesis

Reynolds, S. P. 1986, *ApJ*, 304, 713

Sault, R. J., Teuben, P. J., & Wright, M. C. H. 1995, in *ASP Conf. Ser.* 77: *Astronomical Data Analysis Software and Systems IV*, 433

Simon, M., Ghez, A. M., Leinert, C., Cassar, L., Chen, W. P., Howell, R. R., Jameson, R. F., Matthews, K., Neugebauer, G., & Richichi, A. 1995, *ApJ*, 443, 625

Terebey, S. & Padgett, D. L. 1997, in IAU Symp. 182: Herbig-Haro Flows and the Birth of Stars, 507–514

Tobin, J., Looney, L. W., & Kwon, W. in preparation

Weintraub, D. A., Sandell, G., & Duncan, W. D. 1989, *ApJ*, 340, L69

Welch, W. J., Thornton, D. D., Plambeck, R. L., Wright, M. C. H., Lugten, J., Urry, L., Fleming, M., Hoffman, W., Hudson, J., Lum, W. T., Forster, J. . R., Thatte, N., Zhang, X., Zivanovic, S., Snyder, L., Crutcher, R., Lo, K. Y., Wakker, B., Stupar, M., Sault, R., Miao, Y., Rao, R., Wan, K., Dickel, H. R., Blitz, L., Vogel, S. N., Mundy, L., Erickson, W., Teuben, P. J., Morgan, J., Helfer, T., Looney, L., de Gues, E., Grossman, A., Howe, J. E., Pound, M., & Regan, M. 1996, *PASP*, 108, 93

Wolf-Chase, G. A., Barsony, M., & O’Linger, J. 2000, *AJ*, 120, 1467

Wu, Y., Wei, Y., Zhao, M., Shi, Y., Yu, W., Qin, S., & Huang, M. 2004, *A&A*, 426, 503

Table 1: Positions and simple estimates of mass from the $\lambda = 1.3$ mm continuum.

| Source | α (J2000) ^a | δ (J2000) ^a | Flux (Jy) | Mass (M_{\odot}) | \bar{n}_{H_2} ^b (cm^{-3}) |
|-------------------|-------------------------------|-------------------------------|-------------|----------------------|--|
| L1448 IRS 3A..... | 03 25 36.532 | +30 45 21.35 | 0.196±0.019 | 0.21±0.02 | 3.7×10^7 |
| L1448 IRS 3B..... | 03 25 36.339 | +30 45 14.94 | 1.094±0.027 | 1.15±0.03 | 4.8×10^7 |
| L1448 IRS 3C..... | 03 25 35.653 | +30 45 34.20 | < 0.031 | < 0.03 | < 8.1×10^7 |

^aThe positions are from Looney et al. (2000).

^bMean number density represented by hydrogen molecules. The volumes are estimated as spheres with diameters of 5'', 8'', and 2'' for 3A, 3B, and 3C, respectively.

Table 2: Mass, momentum, and kinetic energy estimates of outflow lobes.

| Lobes ^a | Red-North | Red-East | Black-North | Black-South ^b | Blue-West |
|---|-------------|-------------|--------------------------|--------------------------|-------------|
| Outflow Sources | IRS 3A | IRS 3B | IRS 3A | IRS 3A & 3B | IRS 3B |
| Integrated Flux (Jy km s ⁻¹) | 47.47±1.43 | 101.6±1.55 | 168.7±1.75 | 347.3±2.01 | 304.2±4.36 |
| Mass (10 ⁻³ M _⊙) | 0.153±0.005 | 0.327±0.005 | 0.543±0.006 | 1.12±0.006 | 0.980±0.014 |
| Mean no. density ^c (10 ³ cm ⁻³) | 6.6 | 6.9 | 7.0 | 5.9 | 9.2 |
| Momentum ^d (10 ⁻³ M _⊙ km s ⁻¹) | 1.2 | 3.5 | 0.43, -0.64 ^f | 1.1, -1.1 | -18 |
| Kinetic Energy ^e (10 ⁴¹ erg) | 1.0 | 4.4 | 0.22 | 0.44 | 38 |

^aComponents in Figure 5 as contour colors and positions.

^bThis lobe has two components, one from the IRS 3A outflow and the other from the IRS 3B outflow.

^cMean number density represented by hydrogen molecules. Cylinders along outflows are assumed to estimate the volumes. The assumed diameters and lengths of the cylinders are 5''.5 & 13''.5, 6''.0 & 19''.0, 8''.0 & 17''.5, 11''.0 & 23''.0, and 10''.0 & 15''.5. Note that these are not mean number densities indicating the whole outflow lobes, but partial components of the lobes. For example, the mean number density of the northern lobe of the IRS 3A outflow would be $6.6 + 7.0 = 13.6$ (10³ cm⁻³), assuming the two components occupy the same region.

^dInclination factor, $1/\cos\theta$, is not applied.

^eInclination factor, $1/\cos^2\theta$, is not applied.

^fPlus value is estimated from the redshifted channel and minus from the blueshifted channel.

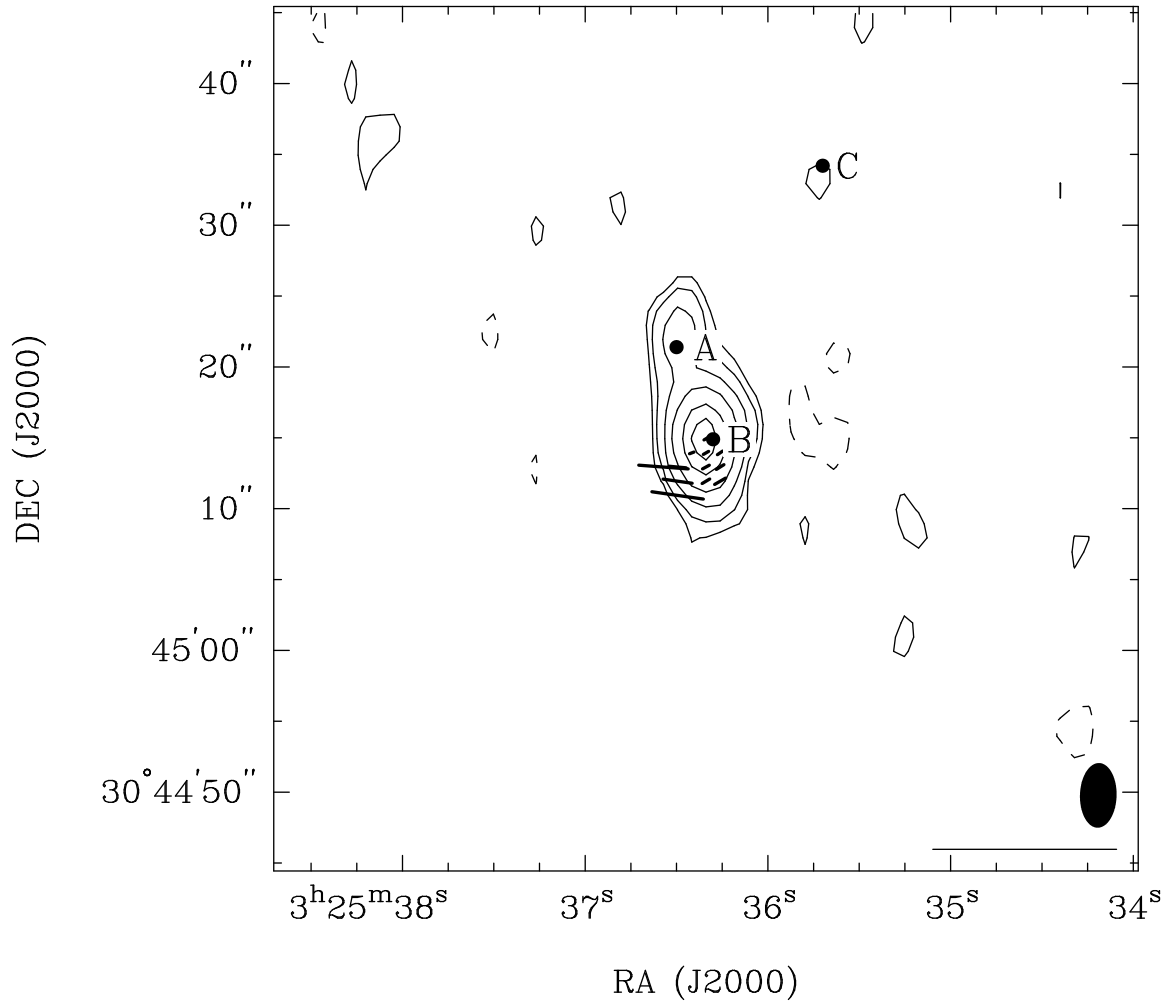


Fig. 1.— $\lambda = 1.3$ mm continuum map of L1448 IRS 3. Vectors indicate linear polarization and the symbols at bottom right show the synthesized beam of $4''.6 \times 2''.6$ (PA = -1.6°) and 100% polarization scale. Contour levels are 3, 5, 10, 20, 40, and 60 times $\sigma = 9.4$ mJy beam $^{-1}$.

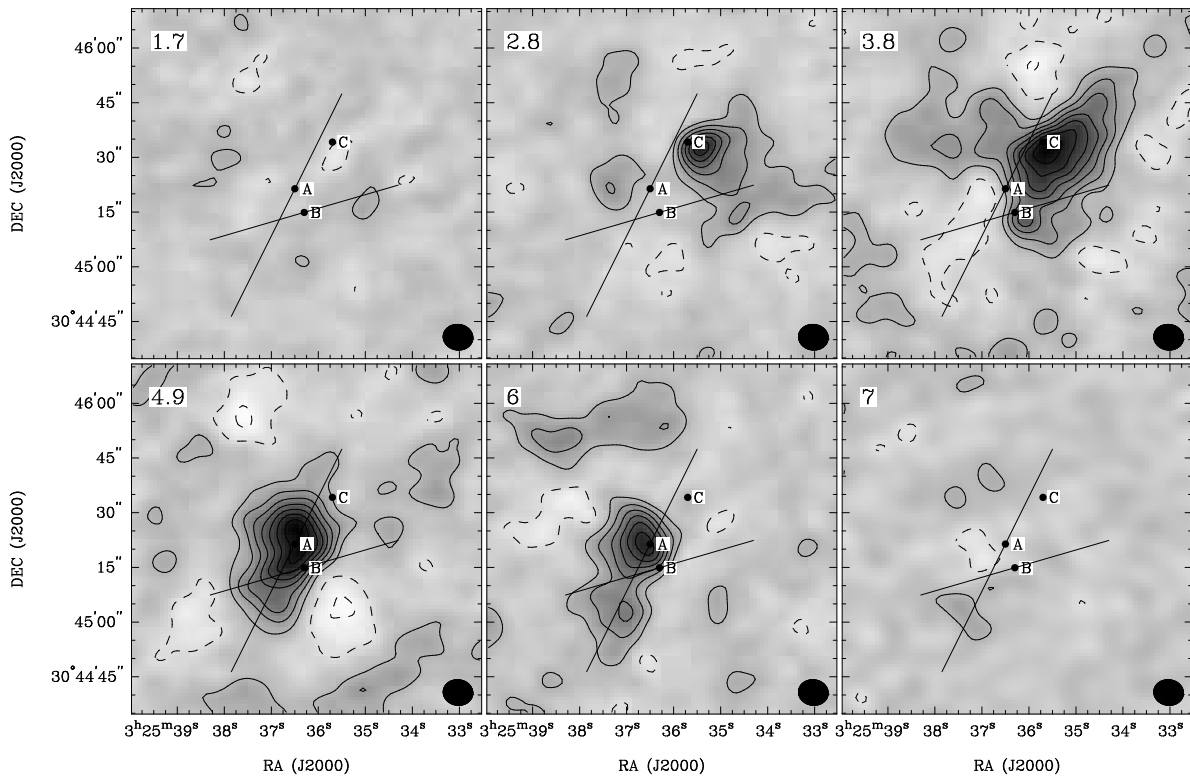


Fig. 2.— ^{13}CO $J = 1 \rightarrow 0$ channel maps of L1448 IRS 3. Two lines indicate the outflow directions that are discussed in §5. Source locations and beam size are marked. The synthesized beam is $8''.1 \times 7''.0$ and PA = 82° . Contour levels are 3, 7, 11, 15, 19, 23, 31, and 35 times $\sigma = 76$ mJy beam $^{-1}$.

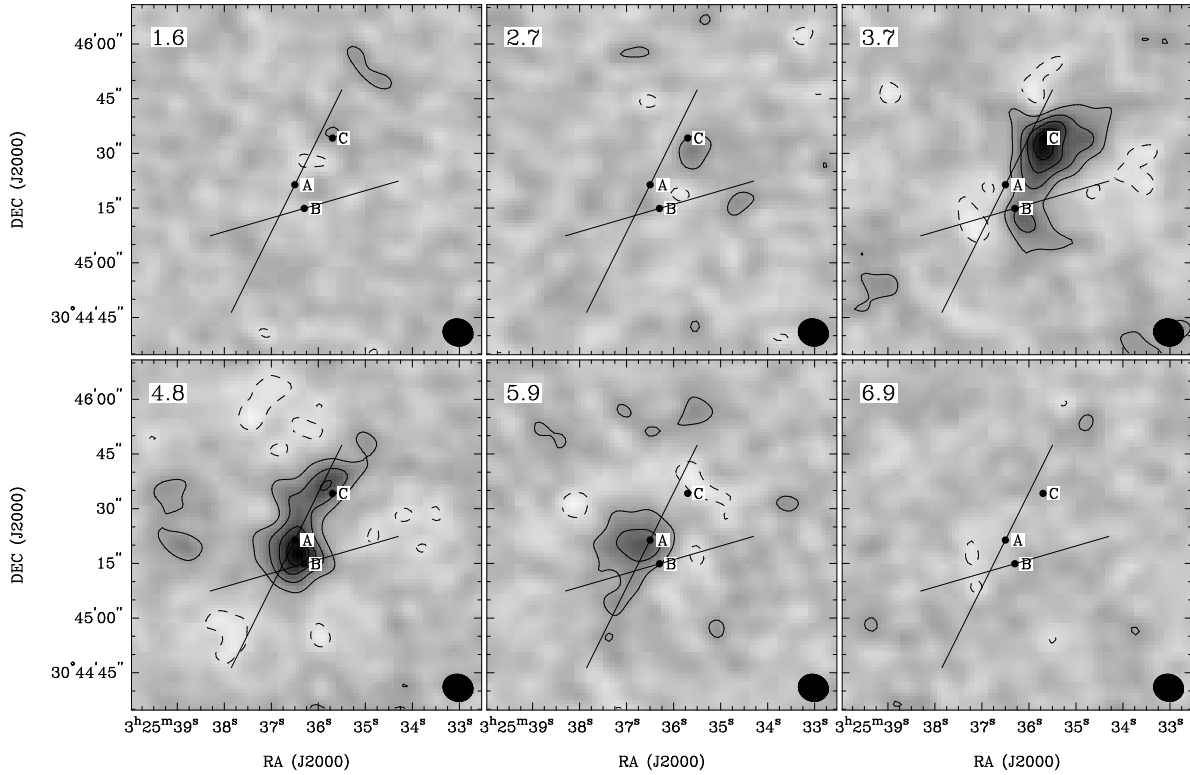


Fig. 3.— C^{18}O $J = 1 \rightarrow 0$ channel maps of L1448 IRS 3. Two lines indicate the outflow directions that are discussed in §5. Source locations and beam size are marked. The synthesized beam is $8''.2 \times 7''.3$ and PA = 72° . Contour levels are 3, 7, 11, and 15 times $\sigma = 76 \text{ mJy beam}^{-1}$.

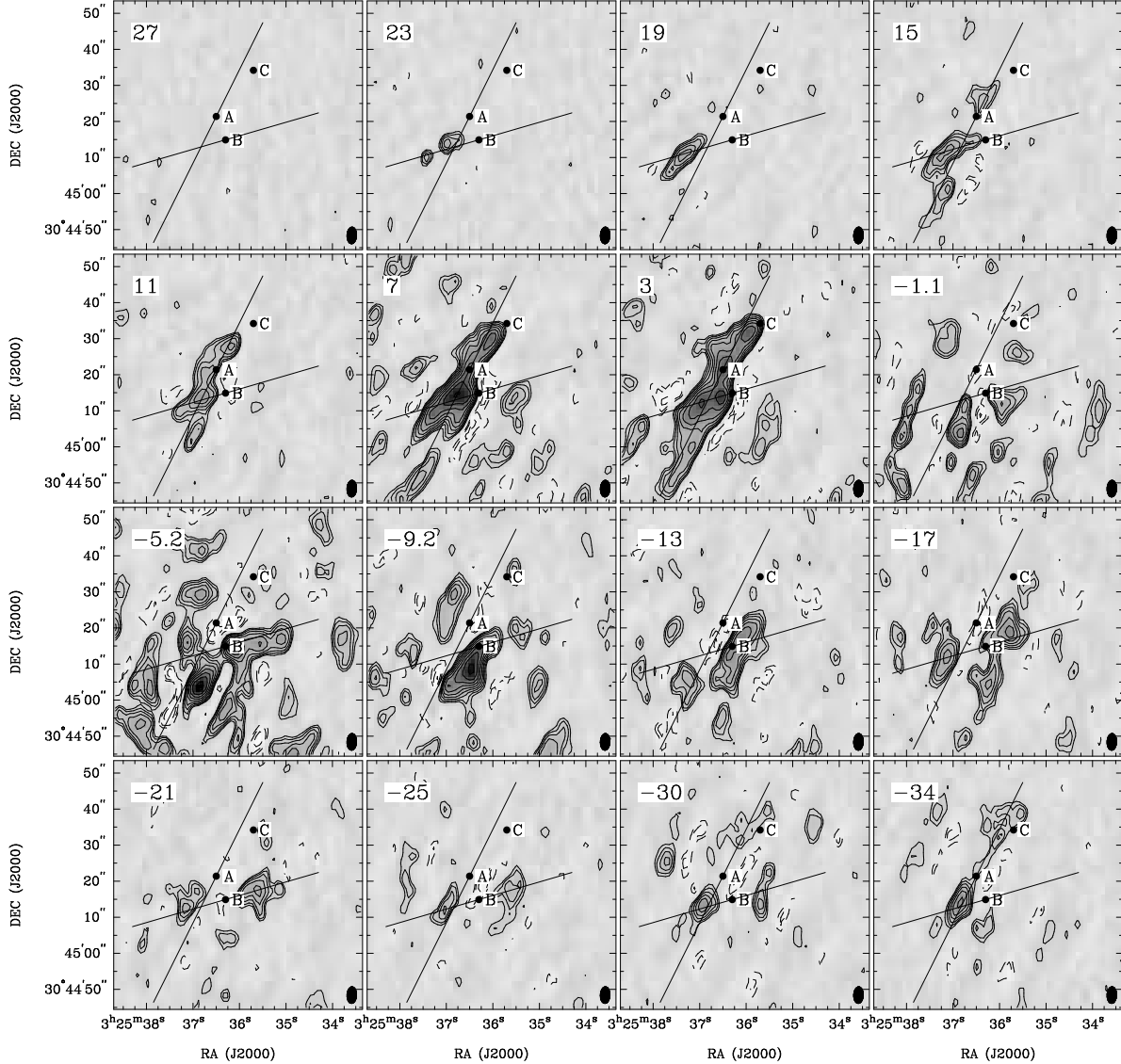


Fig. 4.— CO $J = 2 \rightarrow 1$ channel maps of L1448 IRS 3. Two lines indicate the outflow directions that are discussed in §5. Source locations and beam size are marked. The synthesized beam is $4.5'' \times 2.5''$ and PA = -2.4° . Contour levels are 2.8, 4, 5.7, 8, 11.3, 16, 22.6, 32, and 45.3 times $\sigma = 0.144$ Jy beam $^{-1}$.

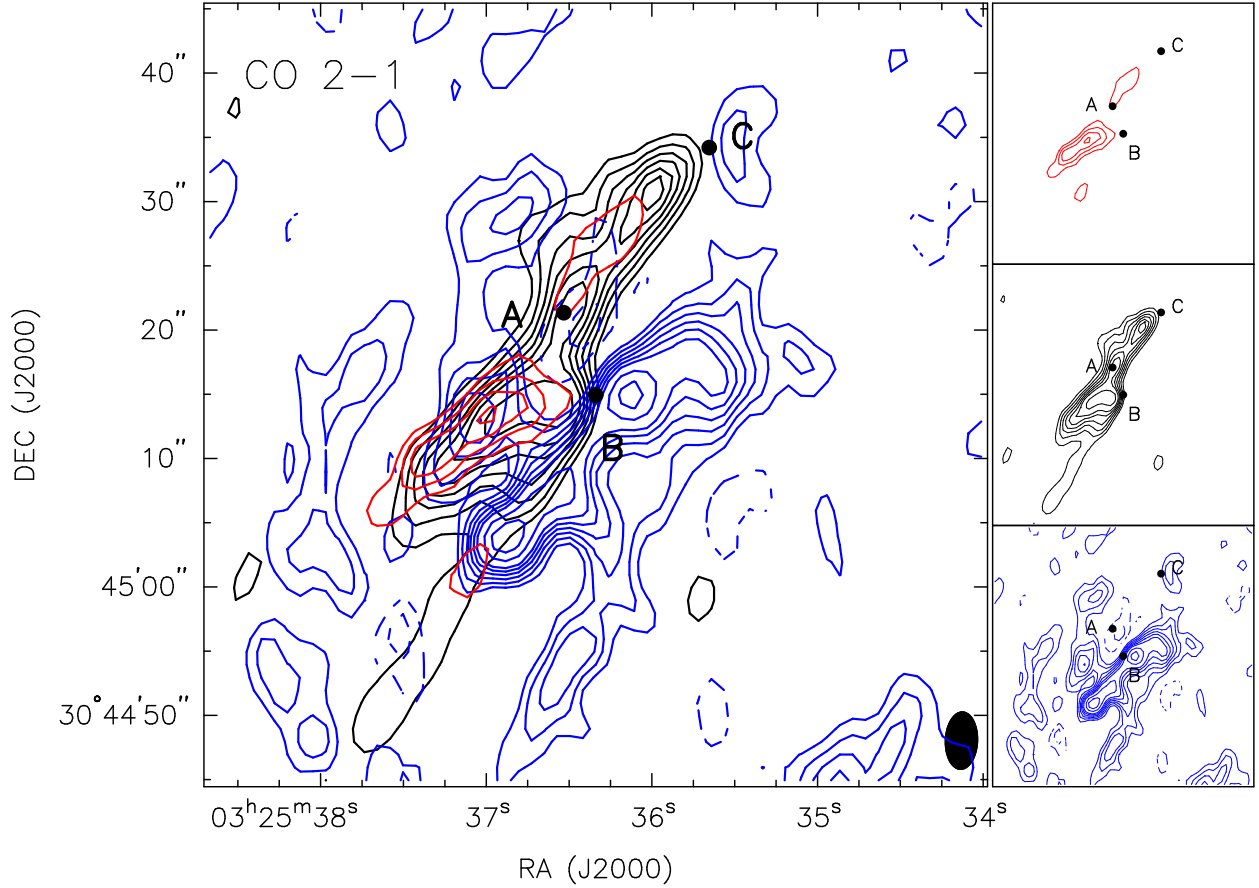


Fig. 5.— Integrated intensity map of L1448 IRS 3. Red, black, and blue contours present velocity ranges from $+25$ to $+9$ km s⁻¹ (4 channels), from $+9$ to $+1$ km s⁻¹ (2 channels), and from $+1$ to -32 km s⁻¹ (8 channels), respectively. The three sub-images on the right have the same velocity ranges as the main panel with the same contour levels, size-scale, etc., but they are separated for easier comparison. The synthesized beam is $4''.5 \times 2''.5$ and PA = -2.4° . Black contours mainly show the IRS 3A outflow and red and blue contours mainly represent redshifted and blueshifted lobes of the IRS 3B outflow. Blue contours look complicated due to blueshifted components of the mm source outflow. Contour levels are 3, 5, 7, 9, 11, 13, 17, 21, 25, 29, 35, 41, and 49 times 2.3 Jy beam⁻¹ km s⁻¹.

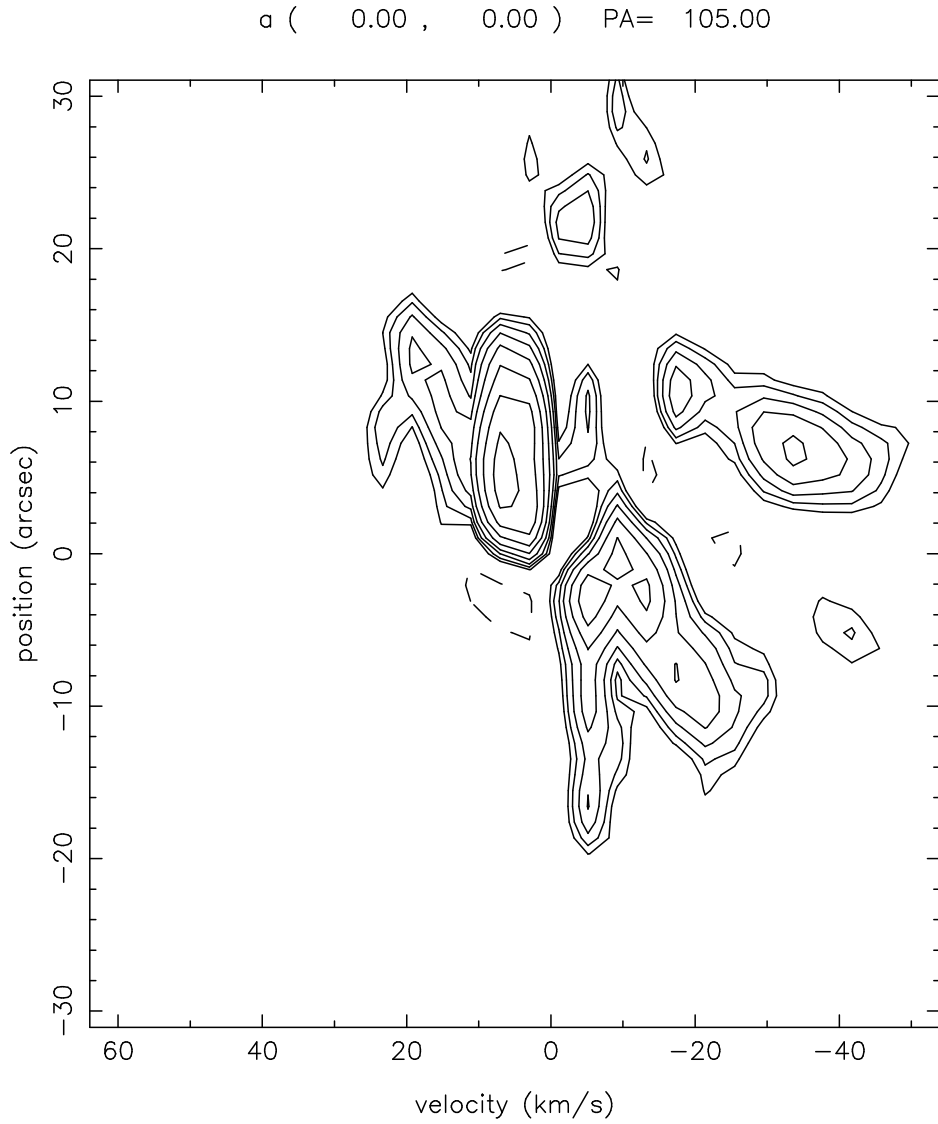


Fig. 6.— Velocity-position diagram of the L1448 IRS 3B outflow. The cut is along 105° from IRS 3B. Contour levels are 2.8, 4, 5.7, 8, 11.3, 16, 22.6, 32, and 45.3 times $\sigma = 0.144$ Jy beam $^{-1}$ same as Figure 4.

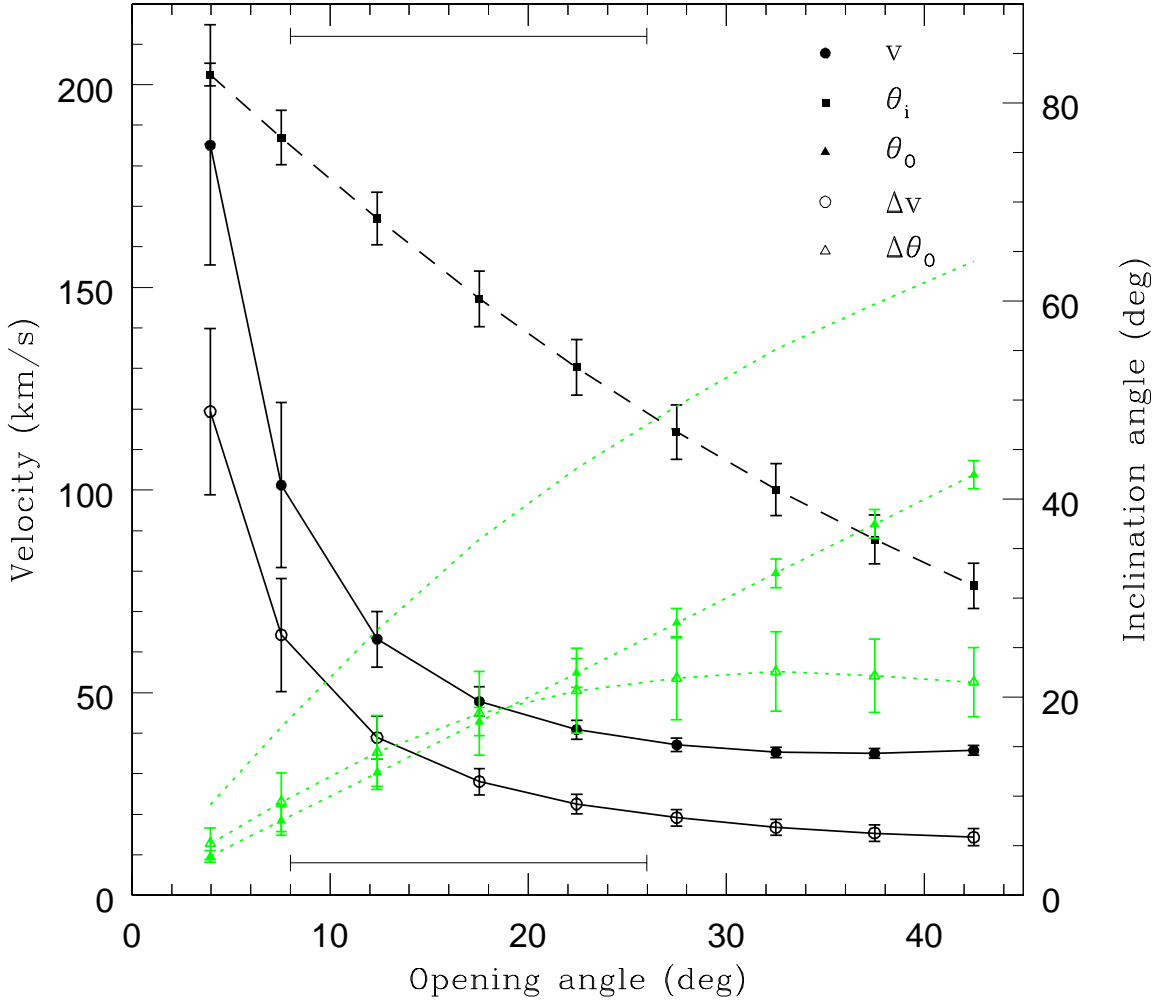


Fig. 7.— Results of searching IRS 3B outflow parameters, velocity (solid circles), inclination angle (solid squares), and velocity and opening angle differences (open circles and open triangles, respectively) versus opening angle. The opening angle is also plotted (solid triangles) to compare with the other parameters. The data points are average values of parameters of samples in 5° bins of the opening angle and the error bars present the standard deviations of the bins. The dotted line without data points indicates the opening angle plus the opening angle difference. The range of the derived opening angles that are consistent with the observations ($8^\circ < \theta_o < 26^\circ$) is indicated by the horizontal bars at the top and bottom of the plot.

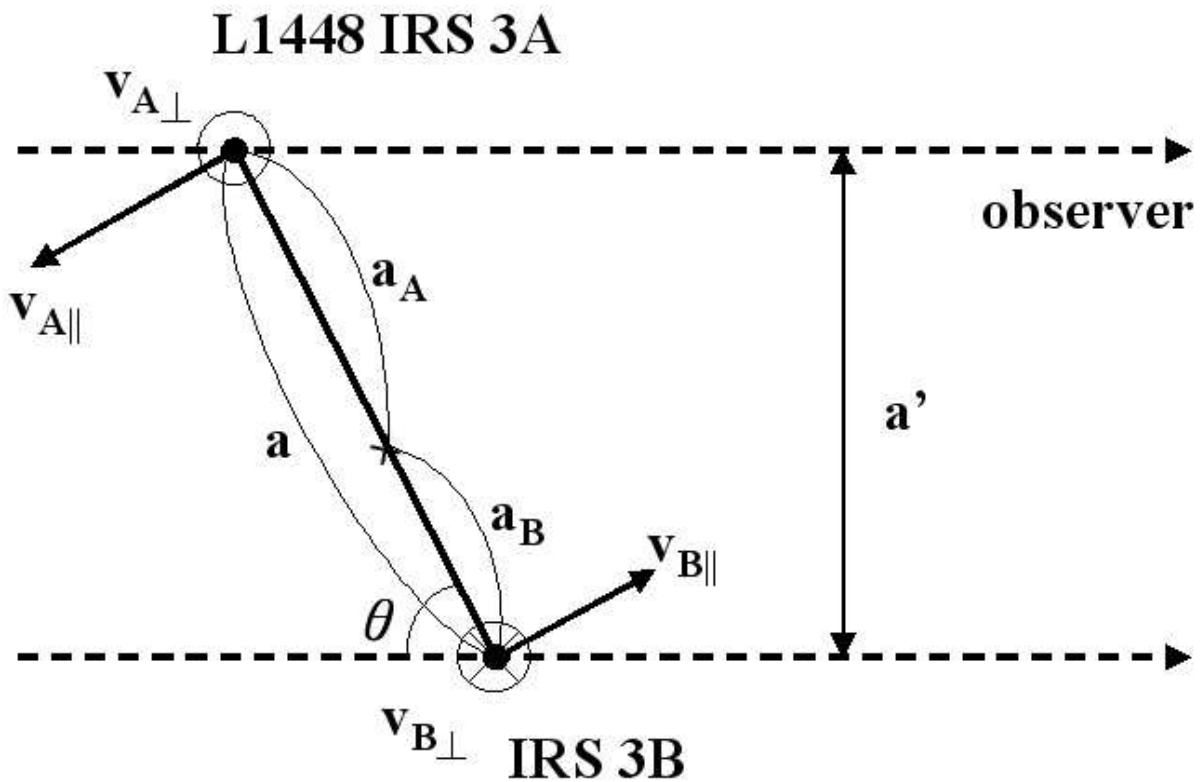


Fig. 8.— Schematic diagram illustrating the binary system of L1448 IRS 3A and 3B. The velocity components vertical to the line-of-sight plane are assumed as forward $v_{A\perp}$ and backward $v_{B\perp}$. They may be opposite directions such as backward $v_{A\perp}$ and forward $v_{B\perp}$.

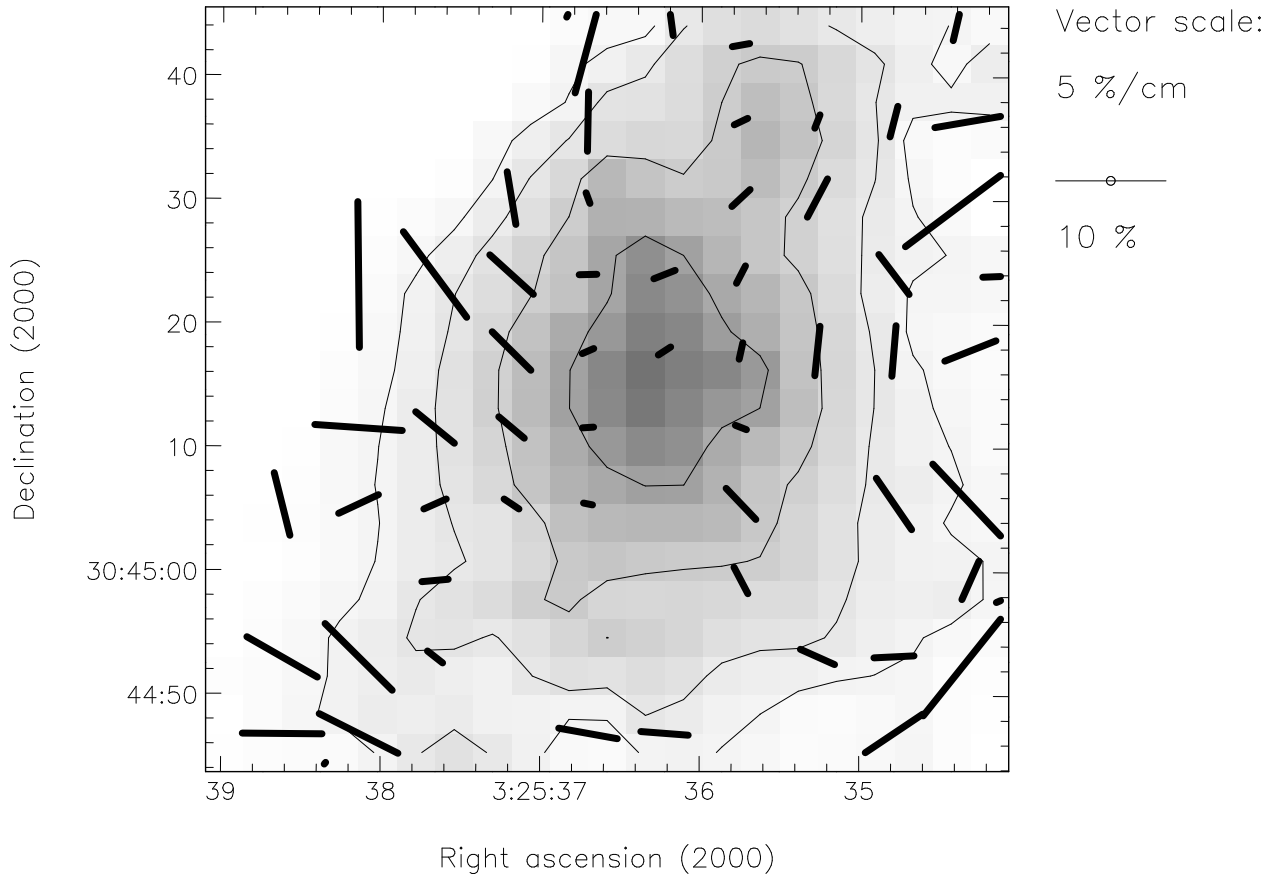


Fig. 9.— Large scale magnetic field in L1448 IRS 3 observed by SCUBA at $\lambda = 850 \mu\text{m}$. Note that vectors indicate linear polarization and the direction around IRS 3B is consistent with our $\lambda = 1.3 \text{ mm}$ continuum data. The beam size is $\sim 13''$. Gray scales and contour levels are 0.9, 0.8, 0.6, and 0.4 of the peak intensity, 6.5 Jy beam^{-1} derived from the data presented in Hatchell et al. (2005).

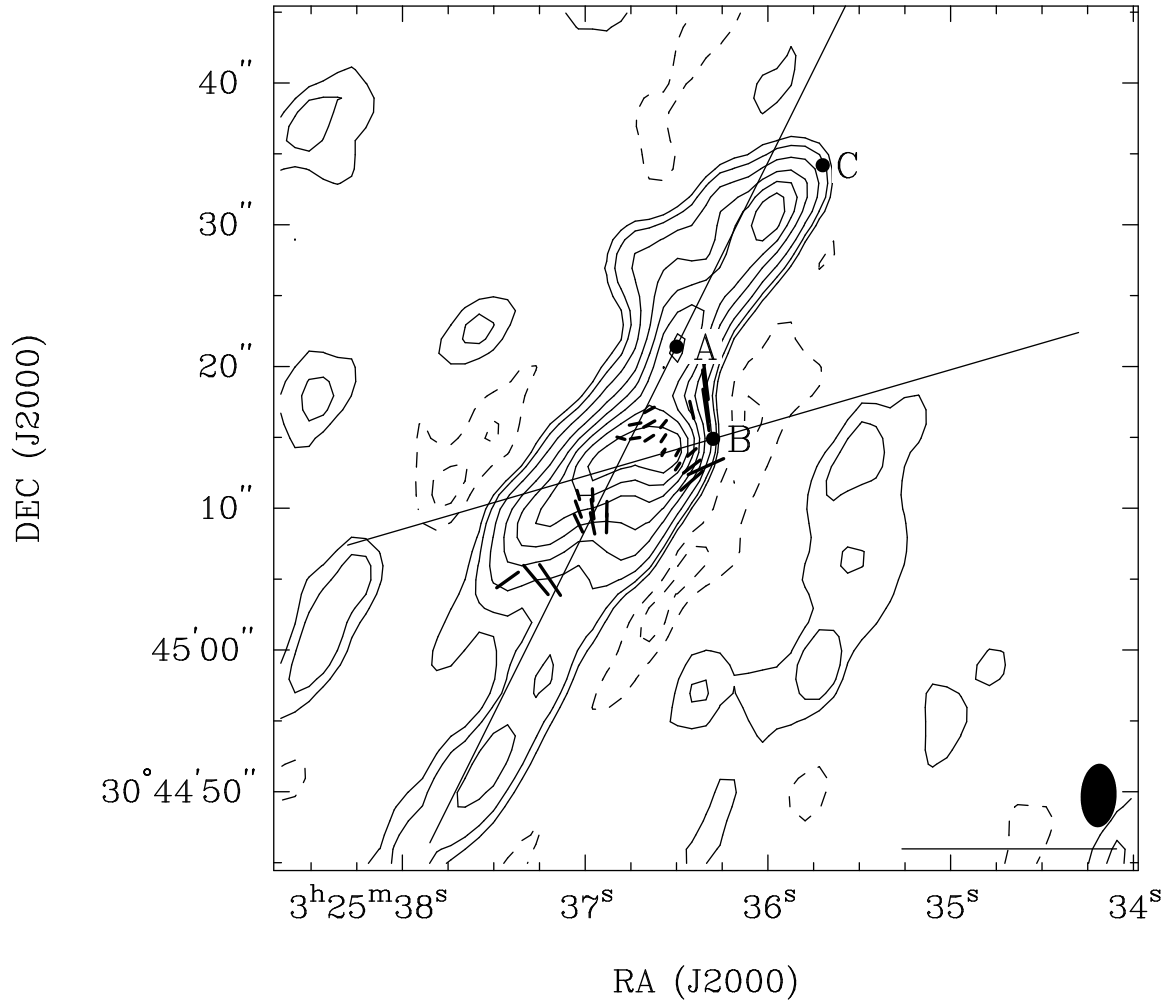


Fig. 10.— CO $J = 2 \rightarrow 1$ map of L1448 IRS 3, combined in two channels, a velocity range from $+1$ to $+9 \text{ km s}^{-1}$. Vectors indicate linear polarization and the symbols at right bottom show the synthesized beam ($4''.5 \times 2''.5$ and PA = -2.4°) and 100% polarization scale. Two lines present outflow directions from IRS 3A and 3B. Contour levels are 3, 5, 9, 15, 21, 27, 33, 39, and 45 times $\sigma = 0.126 \text{ Jy beam}^{-1}$.